RESEARCH ARTICLE

Horizontal meandering in direct numerical simulations of the stable boundary layer

Michel Stefanello[1] ⊙ | **Ricardo A. S. Frantz[2,3]** | **Otávio Acevedo[1]** ⊙ |
Gervasio Degrazia[1] | **Jorge H. Silvestrini[2]**

[1]Departamento de Física, Universidade Federal de Santa Maria, Santa Maria, Brazil

[2]School of Technology, Pontifical Catholic University of Rio Grande do Sul, Porto Alegre, Brazil

[3]Arts et Métiers Institute of Technology, CNAM, DynFluid, HESAM Unisversité, Paris, France

Correspondence
M. Stefanello, Departamento de Física, Universidade Federal de Santa Maria, Santa Maria, Rio Grande do Sul 97105-900, Brazil.
Email: michelstefanello@gmail.com

Abstract

Large-scale nonturbulent motions are investigated using high-resolution direct numerical simulations of the turbulent Ekman layer at a moderate Reynolds number. In particular, the role of stable stratification effects in the generation and amplification of large-scale oscillations in the wind-speed components and buoyancy is analysed. Eulerian autocorrelation functions (EAFs) and spectral analysis help to describe and characterize such modes as meandering-like structures. Focus is given to the strong stability cases, where vertical turbulent motions are damped and large-scale modes drive near-wall patterns of flow laminarization. Horizontal meandering arises in the near-wall region when the ratio of vertical wind-speed variance to horizontal wind-speed variance decreases to small orders of magnitude. In the case of strong stratification, the characteristic features of meandering motion were identified as negative lobes in the EAF, with corresponding low-frequency peaks in the horizontal wind speed and buoyancy spectra. The Ekman configuration used reproduced the development of meandering-like structures satisfactorily in strong stable conditions, as indicated by field observations of the stable boundary layer and its dependence on the level of stratification. At strong stability, the Rotta model constant, which represents the relationship between the dissipation and return to isotropy terms in the velocity variance budget, is shown to vary with stability.

KEYWORDS
direct numerical simulation, Ekman flow, horizontal meandering, stable boundary layer

1 | INTRODUCTION

The dynamics of the atmospheric boundary layer (ABL) are typically driven by turbulent processes that promote the exchange of heat, momentum, water vapour, and other scalars between the surface and the atmosphere, as well as the dispersion of pollutants in this region. At night, however, the cooling of the surface leads to the formation of a stably stratified inversion layer, which suppresses vertical turbulent fluxes. If the stable stratification is strong enough, it can promote the suppression of turbulence in layers of the flow, resulting in large quasi-laminar patches in the near-surface region, ultimately decoupling the inner and outer layers in the vertical direction (Garg *et al.,* 2000; Flores and Riley, 2011; Garcia-Villalba and Del Alamo, 2011; Ansorge and Mellado, 2014; Acevedo *et al.,* 2016; Lan *et al.,* 2018). The processes and interactions that take place in such strongly stratified flows are still not fully understood, imposing difficulties for accurate modelling of turbulent processes in weather

RMetS

forecasting models (Belušić and Güttler, 2010; Steeneveld, 2014). Moreover, the ability of Monin–Obukhov similarity theory to describe turbulence adequately in a strongly stable boundary layer is questionable and an open research topic (see, for example, Mahrt, 2009; 2014 or Sun et al., 2016).

In the seminal study by Nieuwstadt (2005), direct numerical simulations (DNS) in a channel flow configuration were used to investigate the turbulence collapse and relaminarization resulting from strong surface cooling. In a similar setup, Flores and Riley (2011) observed the transition from a turbulent flow to an intermittent/laminar regime, and showed that strong stratification reduces turbulence production near the wall. They also observed that, after turbulence collapses, it becomes intermittent over large flow scales. Similar results were obtained by Iman Gohari and Sarkar (2017) using an Ekman setup. Further DNS studies (Garcia-Villalba and Del Alamo, 2011; Ansorge and Mellado, 2014; Deusebio et al., 2014) have established the simultaneous existence of turbulent patches with laminar flow in the Ekman configuration. Ansorge and Mellado (2014); Ansorge and Mellado (2016) specifically studied the intermittency phenomenon and found an intrinsic link between this phenomenon and strong stable stratification. In this case, intermittency was found to propagate down to the inner layer, regardless of the Reynolds number.

The differences between Ekman layers and channel flow were analysed by Ansorge and Mellado (2014) and Flores and Riley (2018). Unlike the channel flow setup, the Ekman configuration does not exhibit symmetry in the spanwise direction. This is related to the presence of large-scale structures under neutrally stratified conditions (Shingai and Kawamura, 2004), which lead to different outer layers. The inclusion of the Coriolis force plays an essential role in the development of low-level jets and other characteristic large-scale features of the stable boundary layer (SBL) (Ansorge and Mellado, 2014; Shah and Bou-Zeid, 2014; Iman Gohari and Sarkar, 2017). Otherwise, the near-wall regions are very similar, even in nonrotating cases (Jiménez et al., 2009).

Under very stable conditions, weak intermittent turbulence and internal gravity waves (Nappo, 2013) very often coexist with horizontal meandering, a phenomenon characterized by nonturbulent oscillations of the horizontal wind components and temperature (Anfossi et al., 2005; Mortarini et al., 2016b; Cava et al., 2019; Mortarini et al., 2019; Stefanello et al., 2020). Such oscillations are usually studied by means of temporal Eulerian autocorrelation functions (EAFs: Anfossi et al., 2005; Moor et al., 2015; Mortarini and Anfossi, 2015; Mortarini et al., 2016b; Cava et al., 2019; Stefanello et al., 2020; Urbancic et al., 2021) and their implications for the dispersion of pollutants (Carvalho et al., 2005; Anfossi et al., 2006; Vickers et al., 2008; Qian and Venkatram, 2011; Luhar, 2012). The occurrence of horizontal meandering can be identified by a pronounced negative lobe in the EAF, along with a low-frequency energy peak in the horizontal wind velocity and temperature spectra. In such a case, EAFs exhibit oscillatory behaviour that characterizes the presence of wave-like motions with time-scales larger than those of turbulence (Anfossi et al., 2005; Mortarini et al., 2016b; Urbancic et al., 2021). The EAF approach allows estimation of the meandering time-scale as well as the properties of turbulence, and the negative lobe can provide an indication of the importance of oscillation in the flow. The meandering phenomenon is a characteristic feature of the SBL, with particular effects that influence the flow patterns and scalar horizontal dispersion significantly in the presence of weak vertical turbulent mixing (Anfossi et al., 2006; Mahrt and Mills, 2009; Stefanello et al., 2020). Meandering cases often occur at high Richardson number and small magnitudes of the ratio between vertical and horizontal wind-speed variances. Small values of this aspect ratio are indicative of the presence of large anisotropy. The degree of anisotropy in a turbulent flow depends on the interaction between the pressure redistribution and buoyancy terms in the equations for Reynolds stress balances (Bou-Zeid et al., 2018). The redistribution, that is, the linear tendency of turbulence to return to an isotropic state, is a dominant process in the balance of Reynolds stresses and it is usually parameterized using a Rotta-type scheme (see, e.g., Rotta, 1951).

There is no consensus in the literature on the physical causes of meandering formation. For instance, Oettl et al. (2005) suggest that horizontal oscillations are an inherent property of atmospheric flows when turbulent flows are negligible and the flow becomes almost two-dimensional. Theoretical studies by Goulart et al. (2007) have shown that such oscillations are particular solutions of the Navier–Stokes equations, and that they generally do not require a triggering mechanism to develop. It is noteworthy that most previous experimental studies have focused on the use of temporal EAFs to identify meandering cases in large experimental datasets obtained in meteorological towers (e.g., Anfossi et al., 2005; Mortarini and Anfossi, 2015; Moor et al., 2015; Mortarini et al., 2016b; Cava et al., 2019; Stefanello et al., 2020; Urbancic et al., 2021). Such measurements are often made at a single location, spanning only the vertical extension of the observational platforms, which cover only a limited part of the lower ABL.

High-resolution simulations in sufficiently large domains of Ekman flow provided by Ansorge and Mellado (2014); Ansorge and Mellado (2016) have opened

new perspectives for phenomenological studies of the SBL. Their results have shown that intermittency is not necessarily triggered by processes such as low-level jets or surface heterogeneities, but can also be related to large-scale flow structures occurring in the outer regions of the flow. Large-scale modes related to internal gravity waves are a feature of strongly stratified flows, occurring in the core of the channel flow (Garcia-Villalba and Del Alamo, 2011) and in the outer region of the Ekman flow (Shah and Bou-Zeid, 2014).

In the present study, we use the same computational setup as in Ansorge and Mellado (2014) to compute high-resolution direct simulations of a stably stratified Ekman layer. In this sense, the study also aims at expanding the conclusions from Flores and Riley (2011); Ansorge and Mellado (2014; 2016) and Iman Gohari and Sarkar (2017) regarding intermittency on large flow scales to address the meandering phenomenon. It is, therefore, hypothesized here that meandering may also develop naturally as a consequence of intense flow stratification, regardless of the existence of large-scale or external spatial heterogeneities. We focus on the generation and amplification of near-surface large-scale modes under strong stratification and on their characterization as flow meandering. The main objective is to study large-scale oscillations in the horizontal wind components and the buoyancy field under stable thermal stratification. Spatial and temporal Eulerian autocorrelation functions and spatial–spectral analyses of the three velocity components and the buoyancy help to characterize the spatial structures as meandering. Their vertical profiles and dependence on stability conditions are also addressed.

2 | PROBLEM DEFINITION

2.1 | Governing equations

The spatio-temporal evolution of the flow is computed with the nondimensional incompressible Navier–Stokes system of equations for Newtonian fluids, in conjunction with a scalar transport equation for the buoyancy field simplified with the Boussinesq approximation. Following previous works (Coleman *et al.,* 1992; Ansorge and Mellado, 2014; Lee *et al.,* 2020), the equations for the stratified Ekman boundary layer (EBL) problem can be written as

$$\frac{\partial u_i}{\partial x_i} = 0, \tag{1a}$$

$$\frac{\partial u_i}{\partial t} + \frac{1}{2}\left(u_j\frac{\partial u_i}{\partial x_j} + \frac{\partial u_i u_j}{\partial x_j}\right) = \frac{1}{Re}\frac{\partial^2 u_i}{\partial x_j \partial x_j} - \frac{\partial p}{\partial x_i} + f_i + e_i^{\mathrm{g}}bRi, \tag{1b}$$

$$\frac{\partial b}{\partial t} + u_j\frac{\partial b}{\partial x_j} = \frac{1}{Re\cdot Pr}\frac{\partial^2 b}{\partial x_j \partial x_j}, \tag{1c}$$

with x_i, u_i being the spatial and velocity coordinates in the i direction, p being the pressure fluctuation, and t the time.

Alternatively, the velocity vector can be viewed as $\mathbf{u} = (u, v, w)$ evolving in the reference frame $\mathbf{x} = (x, y, z)$, where x and y are the horizontal coordinates and z the vertical coordinate. The equations are nondimensionalized with the Reynolds number $Re = UL/\nu$, with U and L representing characteristic velocity and length scales and ν a (constant) kinematic viscosity coefficient. The buoyancy field coupled via the Richardson number Ri is expressed as $b = \theta'(g/\theta_0)$, where θ' is the fluctuation of the potential temperature field, g is the gravitational acceleration acting on the direction of the unit vector $e_i^{\mathrm{g}} = (0, 0, -1)$, and θ_0 is a background reference temperature. The equations are forced with the vector f_i to account for geostrophic equilibrium.

2.2 | The Ekman scaling

Away from the surface, the flow is in geostrophic balance, that is, the large-scale pressure gradient (spanwise direction y) has the same magnitude as the Coriolis forces f translated by the geostrophic wind G (streamwise direction x). To impose geostrophic balance, the governing equations are forced with

$$f_i = f\epsilon_{i3k}(u_k - G\delta_{k1}), \tag{2}$$

with δ_{k1} being the Kronecker delta, ϵ_{i3k} being the alternating unit tensor, f the Coriolis parameter, and G the geostrophic wind speed.

In neutral stratification, geostrophic balance allows for a statistically steady state. In a fully turbulent state, the flow within the computational domain loses its memory of the initial conditions (decorrelates from the initial conditions), where the dynamics of the Ekman boundary layer at neutral stratification are controlled by the dimensional parameters (G, f, ν, κ).

Despite the interest in fully turbulent states, different studies in the literature (Coleman *et al.,* 1990; Ansorge and Mellado, 2014; Shah and Bou-Zeid, 2014; Iman Gohari and Sarkar, 2017) choose as characteristic length-scale the laminar Ekman-layer depth $D = \sqrt{2\nu f^{-1}}$, leading to the laminar Reynolds number $Re = GD/\nu$. After the initial transients, the flow becomes fully turbulent and reaches a statistically steady state. To account for the change in characteristic scales, the simulations can be rescaled taking into account the thickness of the turbulent Ekman layer δ

and the friction velocity u_*:

$$u_*^2 = \nu \left.\frac{\partial \sqrt{\langle u \rangle^2 + \langle v \rangle^2}}{\partial z}\right|_{z=0}, \quad \delta = \frac{u_*}{f}, \quad (3)$$

which may be used to define the frictional Reynolds number:

$$Re_\tau = \frac{u_* \delta}{\nu}. \quad (4)$$

The vertical variation of the flow velocity is usually characterised by two self-similar regions, namely the inner layer (viscous layer)—dominated by molecular viscosity effects—and the outer layer—dominated by turbulence. The inner and outer layers present different scaling. The statistical normalization expressing inner-layer scaling is performed by ν/u_*, with its quantities being denoted by the superscript $^+$. Quantities described in the outer layer are normalized by the boundary-layer height δ and are denoted by the superscript $^-$. The inner layer refers to those regions at $z^- \leq 0.1$ ($z^+ \leq 50$), and the outer layer to $0.1 < z^- < 1$ ($z^+ > 50$). The quantities $u_{*,N}$ and δ_N refer to the neutral simulation and are used in the normalization of the stratified simulations. Finally, $2\pi f^{-1}$ is adopted as a reference time-scale in the outer regions of the flow.

2.3 | Stable stratification

In the presence of stratification, a buoyancy scale B_0 is also necessary, being defined as the buoyancy difference between the wall and the far field. Here, the stably stratified flow has been simulated using a fixed surface buoyancy (Garcia-Villalba and Del Alamo, 2011; Ansorge and Mellado, 2014; Deusebio et al., 2014; Shah and Bou-Zeid, 2014; He and Basu, 2015). The strength of stratification is governed by the Froude number:

$$Fr^2 = \frac{G^2}{B_0 D}. \quad (5)$$

In the turbulent regime, the stratification can be more appropriately characterized by the global bulk Richardson number:

$$Ri_B = \frac{B_0 \delta}{G^2}. \quad (6)$$

The number of control parameters is reduced by assuming that the Prandtl number $Pr = \nu/\kappa$ (where κ is a constant thermal diffusivity coefficient) equals one.

The stratification in the simulated flow is imposed by applying a Dirichlet boundary condition:

$$\begin{cases} b(x, y, z = 0, t > 0) = 0, \\ b(x, y, z = L_z, t > 0) = B_0. \end{cases} \quad (7)$$

The Obukhov length-scale L_O normalized in wall units (ν/u_*) can be used as an alternative to describe the stratification (Flores and Riley, 2011):

$$L_O^+ = L_O \frac{u_*}{\nu} \equiv \left(-\frac{\theta_0}{g} \frac{u_*^3}{\overline{w'\theta'}\Big|_{z=z_0}} \right) = \left(\frac{u_*^3}{u_* b_*} \right)^+, \quad (8)$$

with

$$u_* b_* = \nu \left.\frac{\partial \langle b \rangle}{\partial z}\right|_{z=0}. \quad (9)$$

From a physical point of view, the length-scale L_O measures the distance a fluid particle may travel until the kinetic energy available in the velocity shear is overcome by the work performed against stratification. In wall-bounded turbulence, this parameter is associated with the gradient Richardson number (Ansorge and Mellado, 2014):

$$Ri_G = \frac{\left.\frac{\partial b}{\partial z}\right|_{z=0}}{\left(\frac{\partial U}{\partial z}\right)^2\Big|_{z=0}} = \nu \frac{b_*}{u_*^3} = \frac{1}{L_O^+}. \quad (10)$$

In the current DNS context, Ri_B is an external control parameter that quantifies the strength of stratification, while Ri_G and L_O^+ are time-dependent quantities that can describe the evolution of flow stratification.

2.4 | Initial and boundary conditions

Given geostrophic balance, the boundary layer that develops in the computational domain is stream- and spanwise-invariant, allowing the use of periodic boundary conditions on the horizontal plane. In the vertical direction, Dirichlet conditions are imposed. For the velocity field, a no-slip condition ($\mathbf{u} = 0|_{z=0}$) is imposed at the bottom and a free-slip boundary condition ($\partial_x u, \partial_y v, w = 0, 0, 0|_{z=L_z}$) at the top of the domain.

In the neutral case, the code must run for a long time before the flow becomes fully turbulent and loses memory of the initial conditions. To shorten the simulation time, we considered the use of mean profiles provided by Ansorge and Mellado (2014) as initial conditions for the neutral simulation. In addition, white noise modulated by the mean turbulent kinetic energy (TKE) profile (also provided by Ansorge and Mellado, 2014) was superimposed on the three velocity fields.

On a fully turbulent, stationary, statistically steady, neutrally stratified flow, a stable buoyancy profile is imposed with a constant temperature at the surface. The initial buoyancy profile is prescribed as

$$b(x, y, z, t_0) = \text{erf}\left[\frac{z/D}{2a}\right] = \text{erf}\left[\frac{z}{2a}\left(\frac{\delta}{\sqrt{2Re_\tau}}\right)^{-1}\right], \quad (11)$$

where b is the buoyancy normalized by B_0, δ and Re_τ are respectively defined in Equations (3) and (4), and $a = 0.15$ is the nondimensional thickness. In the upper part of the computational domain, a Rayleigh-damping layer is imposed along 10 grid points to minimize reflections of large structures. The initial buoyancy profile has a significant role in the initial phase of the simulations, governing the transient time before reaching a quasi-steady state (Ansorge and Mellado, 2014). It can also be observed that the buoyancy field adjusts to the velocity field after a period $ft \approx 1$ and reaches a quasi-equilibrium state (Coleman *et al.,* 1992). Following Shah and Bou-Zeid (2014), statistics are computed in the quasi-equilibrium state (after $ft \approx 6.4$) over half an inertial period. Considering that the system is statistically homogeneous in the horizontal direction, the Reynolds average of a given flow quantity is computed by averaging over horizontal planes (x, y) and is expressed throughout this article by $\langle \bullet \rangle$. Statistics presented in this work have been computed on the fly during the temporal integration of the governing equations. Flow quantities are averaged first on x–y planes along z, and then in time for about half an inertial period (one inertial period is equal to $2\pi f^{-1}$).

3 | NUMERICAL METHODS

3.1 | Flow solver

The direct numerical simulations in this study were performed using the highly parallel open-source finite-differences framework for turbulent flow simulation `Xcompact3D`[1]. The incompressible Navier–Stokes equations coupled with a scalar-transport equation for the temperature are solved on a Cartesian mesh and with high-order finite-difference schemes (Bartholomew *et al.,* 2020). For the spatial discretization, compact sixth-order finite-difference schemes (Lele, 1992) are used, while for the temporal integration an explicit third-order Adams–Bashforth method is used. The divergence-free condition is enforced within the fractional-step method (Chorin, 1968) by solving a Poisson equation directly in spectral space, thanks to efficient 3D fast Fourier transforms. The pressure is calculated in a half-staggered grid arrangement to minimize spurious pressure perturbations (Laizet and Lamballais, 2009). The parallelization is based on a 2D domain decomposition (Laizet and

---

[1]Freely available at http://github.com/xcompact3d/

Li, 2011), where the domain is decomposed into subdomains (pencils), each of which is assigned to an Message-Passing Interface (MPI) process. Thanks to this strategy, `Xcompact3D` can scale strongly with up to hundreds of thousands of computational cores (Laizet and Li, 2011). The `Xcompact3D` framework has been extensively validated and used to compute large-scale DNS and large-eddy simulations in various flow configurations Dairay *et al.* (2014); Dairay *et al.* (2017); Deskos *et al.* (2019); Frantz *et al.* (2021). A Cartesian mesh is stretched to resolve the wall structures better. Details of the stretching function and its spectral requirements can be found in Laizet and Lamballais (2009). The nonlinear term of the momentum equation is computed in the skew-symmetric form, as it is more stable and has less aliasing (Kravchenko and Moin, 1997). The nonlinear term of the scalar transport equation is computed in its nonconservative form, due to the use of different types of boundary conditions for the buoyancy and velocity fields.

3.2 | Simulation overview

In this study, one neutral (N500) and four stratified simulations (W031, I150, S310, and S620, where prefixes W, I, and S refer to weakly, intermediate, and strongly stable stratification) have been performed. Table 1 lists the main parameters of the simulated cases. The simulations were started by the realization of a neutrally stratified flow in which the buoyancy is simulated as a passive scalar, with a subsequent increase of Ri_B. Therefore, a stationary steady fully turbulent flow obtained from the last time step of case N500 is employed to reach the weakly stable case (W031). Accordingly, the final state of case W031 is the initial condition for I150, and this procedure is employed progressively as the stratification increases.

The role of the vertical and horizontal domain sizes in each simulation has been investigated previously by Ansorge and Mellado (2014), who showed that a large domain is necessary to capture the large-scale structures developing in the flow. In the present study, the streamwise and spanwise domain and grid resolution are similar to those in Ansorge and Mellado (2014). The computational grid used is $(1,024)^2 \times 193$. The vertical mesh is stretched in the neutral simulations, with $\Delta z^+|_{z=0} = 1.4$ near the wall and $\Delta z^+|_{z=L_z} = 11$ near the top. No significant difference was observed in the main turbulent and mean statistics when the grid resolution in the viscous sublayer is changed to $\Delta z^+|_{z=0} = 1.05$. The time step in inner coordinates $\Delta t^+ = \Delta t u_*^2/\nu$ for the neutral case is 0.0077, in agreement with Shah and Bou-Zeid (2014).

TABLE 1 Parameters and setup of the DNS case

Case	Re	Fr^2	Ri_B	L_{xy}/D	L_{xy}/δ	L_z/D	L_z/δ	Δx^+	Δy^+	$\Delta z^+\|_{z=0}$
N500	500	∞	0	135	8.6	57	3.6	4.1	4.1	1.4
W031	500	500	0.031	135	8.6	57	3.6	4.1	4.1	1.4
I150	500	100	0.15	135	8.6	57	3.6	4.1	4.1	1.4
S310	500	50	0.31	135	8.6	57	3.6	4.1	4.1	1.4
S620	500	25	0.62	135	8.6	57	3.6	4.1	4.1	1.4

Note: In the name of the case, N, W, I, and S denote neutral, weak, intermediate, and strong stratification classes, respectively.

3.3 | Validation

In this section, the results of the neutrally stratified case are compared with other DNS studies to validate the current code. It has been shown that the Reynolds number $Re = 500$, although small, is in the turbulent range. Previous studies (Ansorge and Mellado, 2014; Shah and Bou-Zeid, 2014) have shown that this is sufficient to distinguish between the inner and outer scales of the Ekman layer. The wall-friction velocity u_{*N} (Equation 3) and the veering angle α of the surface stress with respect to the geostrophic wind G are usually regarded as parameters through which the simulations results may be compared (Coleman *et al.*, 1990; Ansorge and Mellado, 2014; Shah and Bou-Zeid, 2014; Iman Gohari and Sarkar, 2017). Ansorge and Mellado (2014) found $u_{*N} = 0.0618$ and $\alpha = 25.5°$ for the case $Re = 500$, both values in good agreement with those from the present DNS: $u_{*N} = 0.0622$ and $\alpha = 24.5°$.

Both the velocity hodograph (Figure 1a) and the mean horizontal velocity (Figure 1b) compare well with those from Ansorge and Mellado (2014). Furthermore, in agreement with Coleman (1999), Miyashita *et al.* (2006), and Ansorge and Mellado (2014), a logarithmic mean velocity U^+ profile is found at about $z^+ = 30$ (Figure 1b).

At $z^- = 0.12$ (shown as a diamond in Figure 1b), the velocity profile departs from the log law as it begins to turn towards the geostrophic wind direction (Tennekes, 1984; Ansorge and Mellado, 2014; Shah and Bou-Zeid, 2014; Iman Gohari and Sarkar, 2017). The turbulent kinetic energy (TKE) profile in the neutral case also agrees well with those from Ansorge and Mellado (2014) (Figure 1c). The TKE profiles from the present study peak at $z^+ = 16.15$.

Consider the TKE budget equation:

$$\frac{\partial e}{\partial t} + \langle u \rangle_j \left(\frac{\partial e}{\partial x_j} \right) = \Pi + T + P + D - \epsilon, \quad (12)$$

where $e = \frac{1}{2} \langle u_i' u_i' \rangle$ is the turbulent kinetic energy,

$$\Pi = -\frac{1}{\langle \rho \rangle} \frac{\partial \langle p' w' \rangle}{\partial z}$$

is the pressure transport term,

$$T = -\frac{1}{2} \frac{\partial \langle u_i' u_i' w' \rangle}{\partial z}$$

is the turbulent transport term,

$$P = -\langle u_i' w' \rangle \left(\frac{\partial \langle u_i \rangle}{\partial x_j} \right)$$

is the shear production term,

$$D = \nu \frac{\partial^2 \langle u_i' u_i' \rangle}{\partial z^2}$$

is the viscous diffusion term and

$$\epsilon = 2\nu \left\langle \left(\frac{\partial u_i'}{\partial x_j} \right) \left(\frac{\partial u_i'}{\partial x_j} \right) \right\rangle$$

is the viscous dissipation rate. The budget terms are very similar to those calculated by both Ansorge and Mellado (2014) (Figure 1d) and Shah and Bou-Zeid (2014). The shear production, turbulent transport, and viscous diffusion terms peak in the inner layer near the same height, close to $z^+ = 12$. Near the surface ($z^+ < 5$), energy is provided to the system from downward viscous diffusion originating from the buffer layer that dissipates locally. In the region of high turbulence production ($8 < z^+ < 16$), turbulent transport contributes to TKE reduction. A balance between shear production and viscous dissipation processes becomes dominant above $z^+ = 30$.

4 | RESULTS

4.1 | Stratified turbulent Ekman flow

An initial decay and subsequent recovery of u_*/G occurs in all simulations (except the neutral case N500), as the flow is subject to different stratification intensities (Figure 2). For the most stable cases (S310 and S620), the initial u_*/G
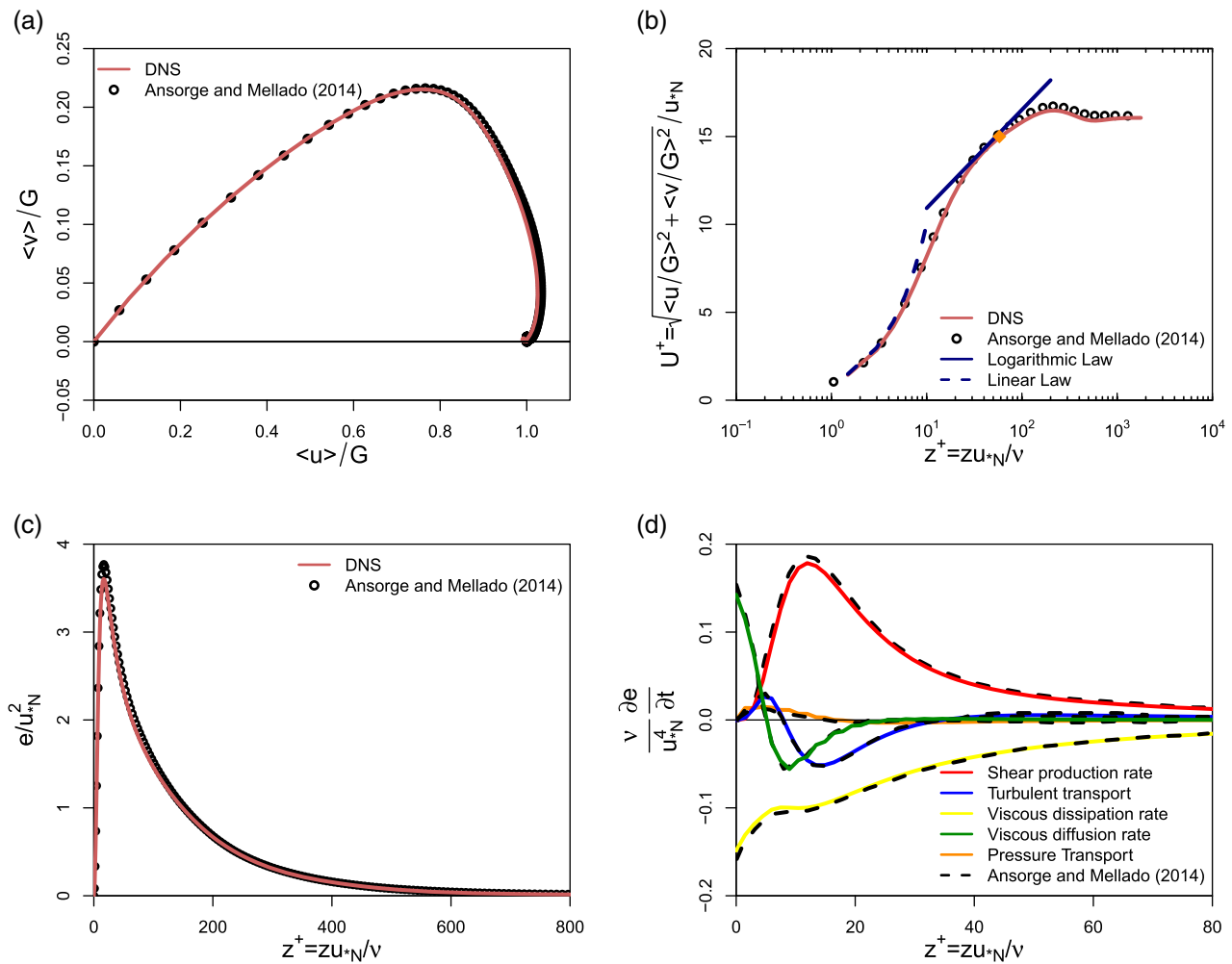
FIGURE 1 Vertical profiles of (a) velocity hodograph, (b) mean velocity and the logarithmic law: $U^+ = (1/\kappa)\log z^+ + B$, with U representing the mean horizontal velocity, $\kappa = 0.41$, and $B = 5.33$, where the level $z^- = z/\delta_N = 0.12$ is also indicated as a orange diamond symbol in the velocity profile, (c) TKE, and (d) TKE budget terms normalized by u_{*N}^4/ν in comparison with Ansorge and Mellado (2014) [Colour figure can be viewed at wileyonlinelibrary.com]
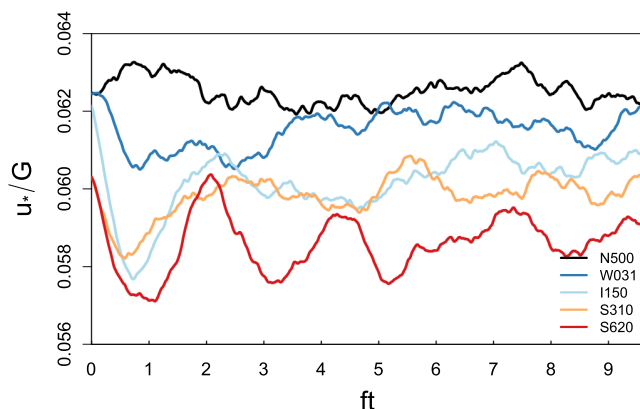
FIGURE 2 Temporal evolution of the normalized friction velocity (u_*/G) for different stratification levels [Colour figure can be viewed at wileyonlinelibrary.com]

recovery is followed by subsequent fluctuations of this variable along the entire simulation, a result also previously reported by Shah and Bou-Zeid (2014).

The spatial distribution of u_*/G at specific times displays the natural occurrence of clusters of turbulent activity, which are more evident as the flow gets more stable (Figure 3). In the very stable case, large quiescent regions with reduced u_*/G occur in the neighbourhood of turbulent wakes, associated with near-laminar conditions. Ansorge and Mellado (2016) reported similar patterns, associating the localized clusters of turbulence with intermittency (Mahrt, 1999) and suggesting that they are related locally to large-scale patterns of flow laminarization. At the same, it is noteworthy that such localized pockets of turbulence are characterized by a low-frequency temporal fluctuation of flow variables, such as u/G (Figure 3d–f) and v/G (Figure 3g–i). These time series are qualitatively similar to those reported along
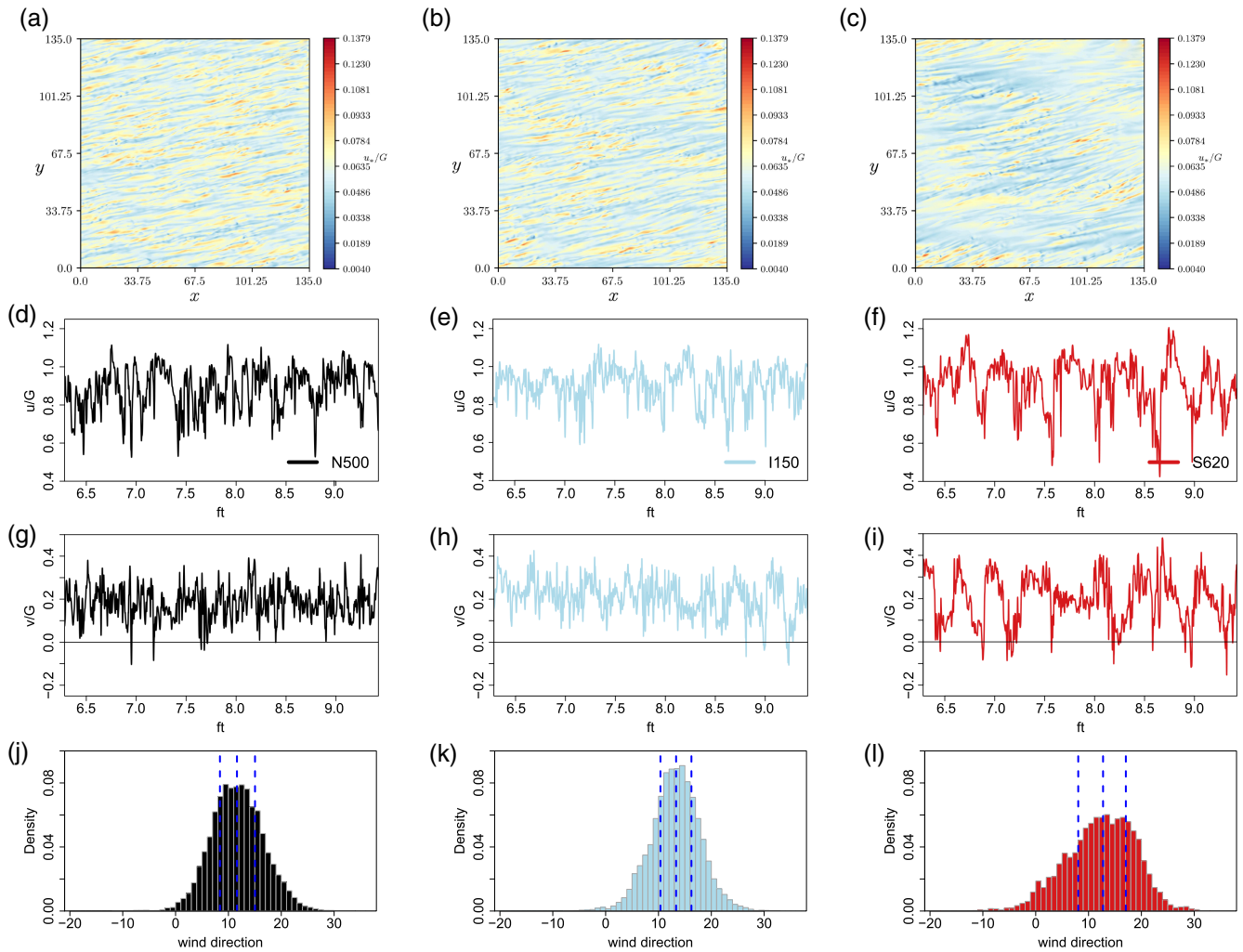
FIGURE 3 Friction velocity (u_*/G) at $ft \approx 9.5$ for different stability regimes. From left to right: (a) neutral, N500; (b) intermediate, I150; (c) strong stable, S620. Time series of streamwise velocity component (d)–(f), spanwise velocity component (g)–(i), and frequency distributions of wind direction (j)–(l) obtained in the centre of the horizontal domain in the inner layer at $z^- \approx 0.1$, for neutral, N500 (black), intermediate, I150 (light blue), and strong stable, S620 (red) cases. The vertical blue dashed lines denote the second quantile, median, and fourth quantile [Colour figure can be viewed at wileyonlinelibrary.com]

meandering occurrences (Mortarini *et al.,* 2016b; Mortarini *et al.,* 2018; Cava *et al.,* 2019), when low-frequency fluctuations are superposed on high-frequency turbulent variability. During meandering, the flow direction typically varies greatly, often spanning all quadrants (Anfossi *et al.,* 2005). Although this is not the case in the present DNS, it is clear that the flow spans a larger range of directions in the very stable case (Figure 3l) than in the others (Figure 3j,k).

In the neutral case, the mean velocity profile is maximum in the outer layer near $z^- = 0.45$ (Figure 4a). With increasing stratification, the height of such a maximum approaches the surface and occurs below $z^- = 0.28$ in the most stable case. This is consistent with the reduction of the turbulent momentum flux near the wall due to buoyancy (Shah and Bou-Zeid, 2014). Figure 4b shows that the TKE decreases at all heights with increasing stability from the neutral (N500) to the intermediate case (I150). On the other hand, as stability increases further (cases S310 and S630), larger TKE values occur above the near-surface peak, even exceeding those found in the neutral reference profile (N500). Ansorge and Mellado (2014); Ansorge and Mellado (2016) suggested that such a TKE increase in very stable cases is associated with large-scale modes, possibly related to gravity waves. The TKE buoyancy destruction increases with stratification, with a maximum near the surface, the height of which increases slightly with stratification (Figure 4c). Accordingly, the largest values of buoyancy variances occur in the most stable simulations (Figure 4d), but in this case the profiles show a vertical maximum away from the surface, which is also discussed in Section 5.
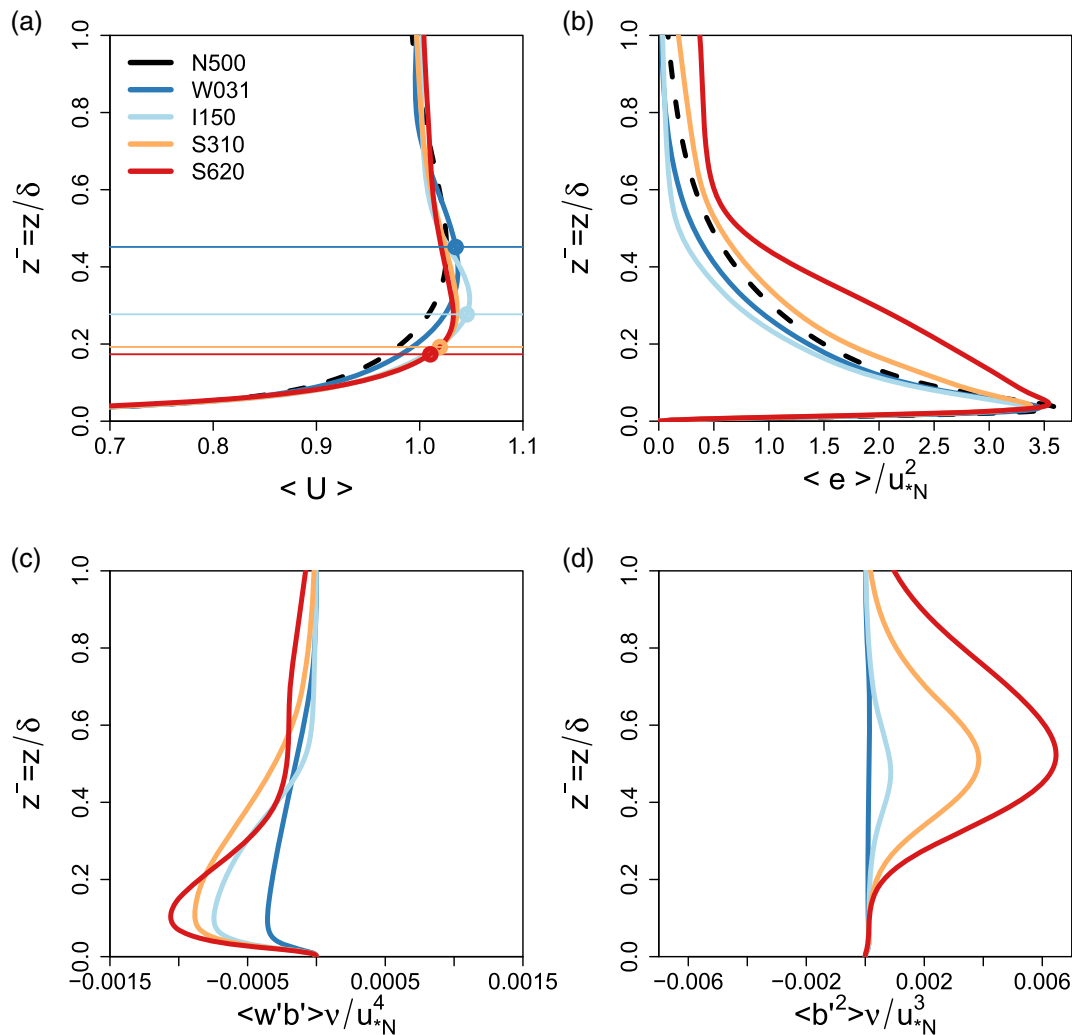
FIGURE 4 Vertical profiles showing the behaviour of (a) mean velocity, (b) TKE, (c) buoyant destruction, and (d) buoyancy variance (buoyancy destruction term of $<w'b'>$ budget). The horizontal lines in the panel (a) indicate the height ($z^- = 0.45, 0.28, 0.20, 0.17$) at which the gradient Richardson number (Ri_G) reaches the critical value of 0.25 [Colour figure can be viewed at wileyonlinelibrary.com]

Regarding the velocity variances, close to the surface (inner layer, $z^- < 0.1$), the vertical velocity variance (σ_w^2/u_{*N}^2, Figure 5b) decreases with increasing stability with respect to the neutral profile. A slight reduction is also observed for the horizontal velocity variance (σ_H^2/u_{*N}^2, Figure 5a), but only until the stability reaches its intermediate value, in case I150. Further away from the surface (in the outer layer), on the other hand, both σ_H^2/u_{*N}^2 ($z^- > 1$) and σ_w^2/u_{*N}^2 ($z^- > 0.25$) are generally larger in the most stable case (S620) than in all other cases. For σ_H^2/u_{*N}^2, the deviation from the neutral profile in the outer layer depends on both height and stratification. It is noteworthy that there is a minimum of σ_H^2 and σ_w^2 for case I150. This is the stability range at which the regime changes from weak to strong stability, also coinciding with the maximum buoyancy flux. This also indicates that the large variance values for the more stratified cases may

be due to wave-like activity. The effect of the stratification in damping vertical fluctuations with respect to those of the horizontal velocity components can be seen in Figure 5c. The aspect ratio shown in this panel equals unity for isotropic turbulence, when all three velocity variances are the same. Mahrt (2011) found that this ratio has an upper limit for very stable conditions close to 0.7, a value that is reached near the surface in the neutral and weakly stable simulations. As stability increases, it is possible to distinguish two patterns vertically: below $z^- \approx 0.3$ the aspect ratio for the most stable cases is smaller than in the neutral case, while the opposite occurs above this height. Small aspect ratios, such as those that occur below $z^- \approx 0.3$ in the most stable cases, indicate accentuated spatial anisotropy (Luhar et al., 2009) and the presence of horizontal meandering structures (Mortarini et al., 2019).

FIGURE 5 Vertical profiles showing the behaviour of (a) horizontal and (b) vertical velocity variance, and (c) the aspect ratio (vertical lines represent 0.7 (dashed) and 1 (continuous)) [Colour figure can be viewed at wileyonlinelibrary.com]
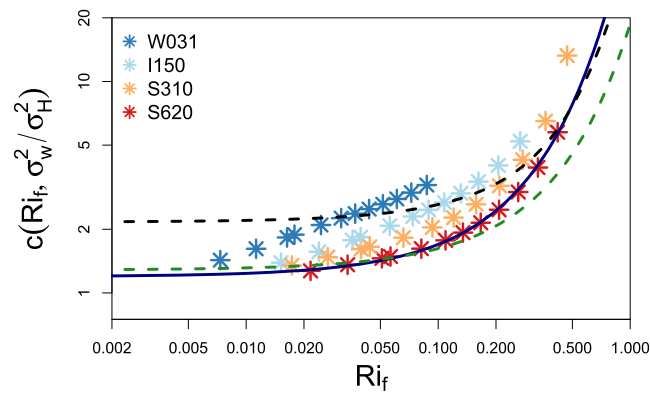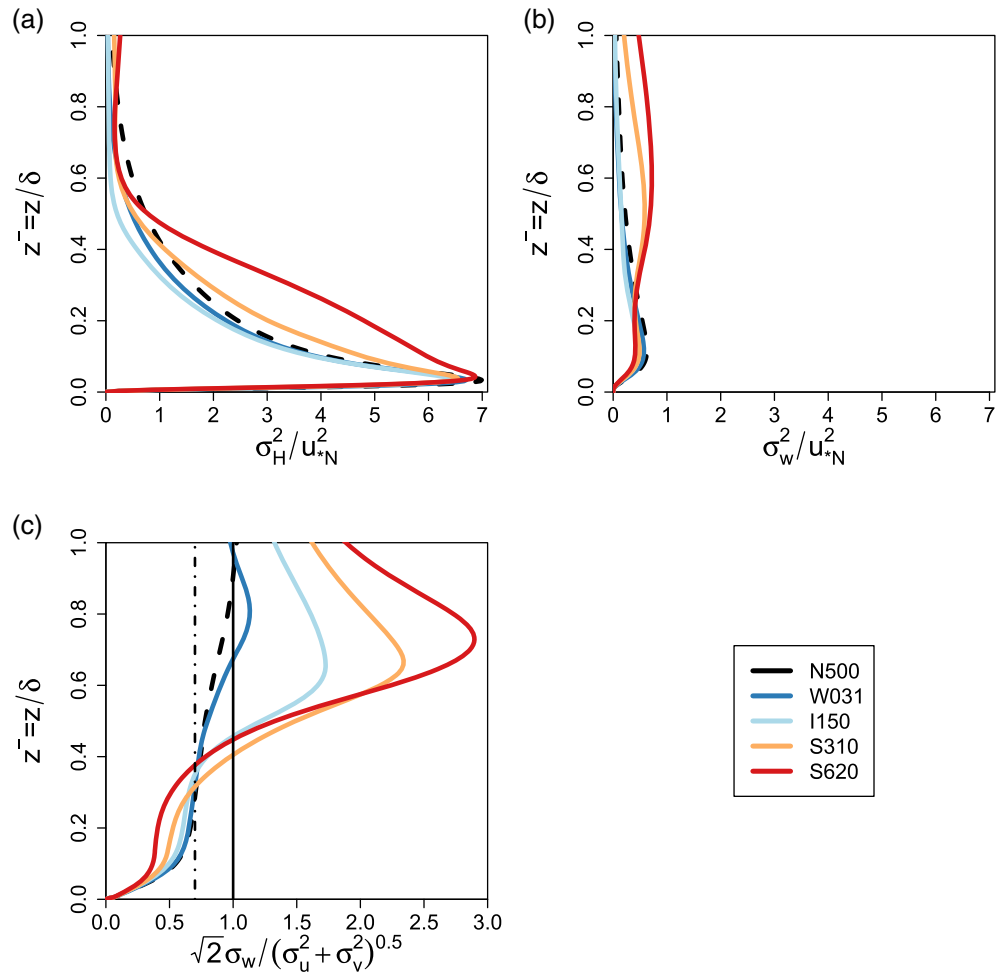

FIGURE 6 Parameter c calculated from Equation (15) in the range $0.07 < \bar{z} < 0.3$ as a function of the flux Richardson number (Ri_f) for the different stable simulations. The continuous blue line refers to the nonlinear best fit of the data ($0.196 + e^{(4.059Ri_f)}$), while the green (meandering) and black (nonmeandering) dashed lines correspond to the expressions proposed by Mortarini et al. (2019) [Colour figure can be viewed at wileyonlinelibrary.com]

4.2 | Large-scale meandering-like structures and isotropy

At high Richardson numbers, negative buoyancy inhibits vertical turbulent motions, resulting in highly anisotropic and intermittent turbulence (Stiperski and Calaf, 2018; Mortarini et al., 2019). Large-scale motions can alter the isotropy of the turbulence further (Stiperski and Calaf, 2018). Since the main source of vertical turbulence under stable conditions is the pressure redistribution term, the degree of anisotropy depends on the interaction between this term and the buoyancy terms (Bou-Zeid et al., 2018). The turbulence anisotropy represents an additional complexity in the parameterization of turbulence in numerical atmospheric models (Stiperski and Calaf, 2018; Vercauteren et al., 2019). Following Mortarini et al. (2019) and assuming an equilibrium between the TKE production rate and the TKE dissipation rate, the ratio σ_w^2/σ_H^2 can be expressed as follows:

$$\frac{\sigma_w^2}{\sigma_H^2} = \frac{-Ri_f + \frac{1}{3}(c-1)(1-Ri_f)}{1 + \frac{2}{3}(c-1)(1-Ri_f)},\tag{13}$$
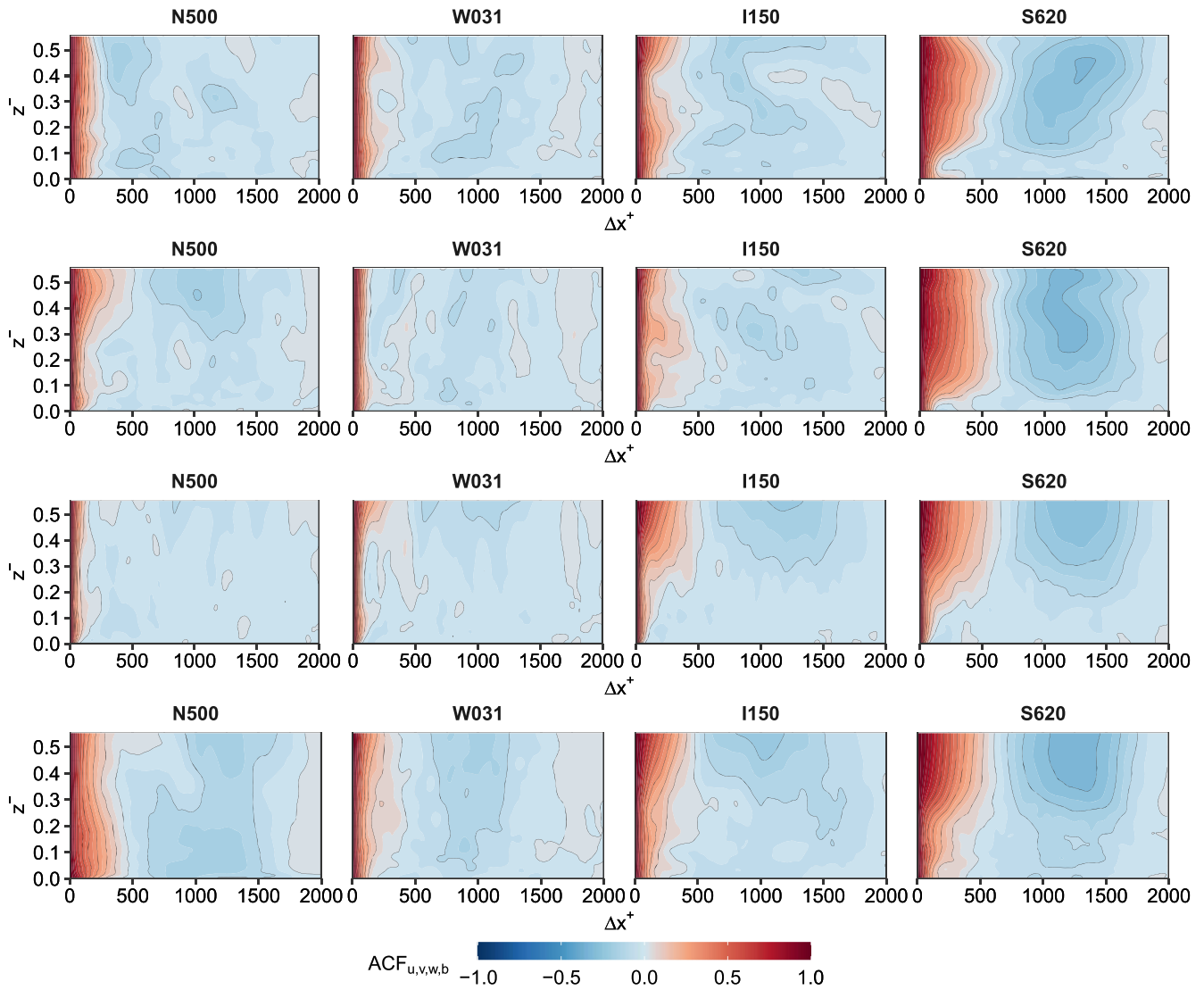
FIGURE 7 Eulerian autocorrelation function for the wind-velocity components u (first line) and v (second line), w (third line), and buoyancy b (fourth line). Each column indicates different stability intensities [Colour figure can be viewed at wileyonlinelibrary.com]

where Ri_f is the flux Richardson number:

$$Ri_f = \frac{g}{\theta_0} \frac{w'\theta'}{\left(u'w'\frac{\partial u}{\partial z} + v'w'\frac{\partial v}{\partial z}\right)}, \quad (14)$$

and the parameter c is associated with a Rotta-type closure for the pressure redistribution terms, expressing the relationship between dissipation and return to isotropy. An expression for c can be derived with Equation (13) as a function of Ri_f in the form:

$$c\left(Ri_f, \frac{\sigma_w^2}{\sigma_H^2}\right) = \frac{1 + \frac{\sigma_w^2}{\sigma_H^2} + 2\frac{\sigma_w^2}{\sigma_H^2}Ri_f + 2Ri_f}{1 - 2\frac{\sigma_w^2}{\sigma_H^2} + \frac{\sigma_w^2}{\sigma_H^2}Ri_f - Ri_f}. \quad (15)$$

Figure 6 exhibits c values provided by Equation (15) as a function of the Richardson number, evaluated in the region $0.07 < z^- < 0.3$. One can observe a good agreement between the strongly stable simulation (S620) and the observations described by Mortarini *et al.* (2019) under meandering conditions, fitted by the function $c(Ri_f) = a + e^{bRi_f}$. Data from the other stratifications show different dependences of c on Ri_f

The nonlinear best-fitting equation for the S620 simulation outputs is shown at the top of Figure 6, with a and b values of 0.196 and 4.059, respectively. They are close to the median experimental values $a = 0.284$ and $b = 2.91$ obtained by Mortarini *et al.* (2019). The best-fitting equation from the DNS data predicts a neutral limit of $c \approx 1.2$ as $Ri_f \to 0$. This value is lower than the one usually found in the literature for the Rotta constant ($c = 1.8$: Pope, 2000), but it is remarkably close to that estimated from the data during meandering conditions with $c \approx 1.3$. For larger values of Ri_f, at the very stable limit, the points
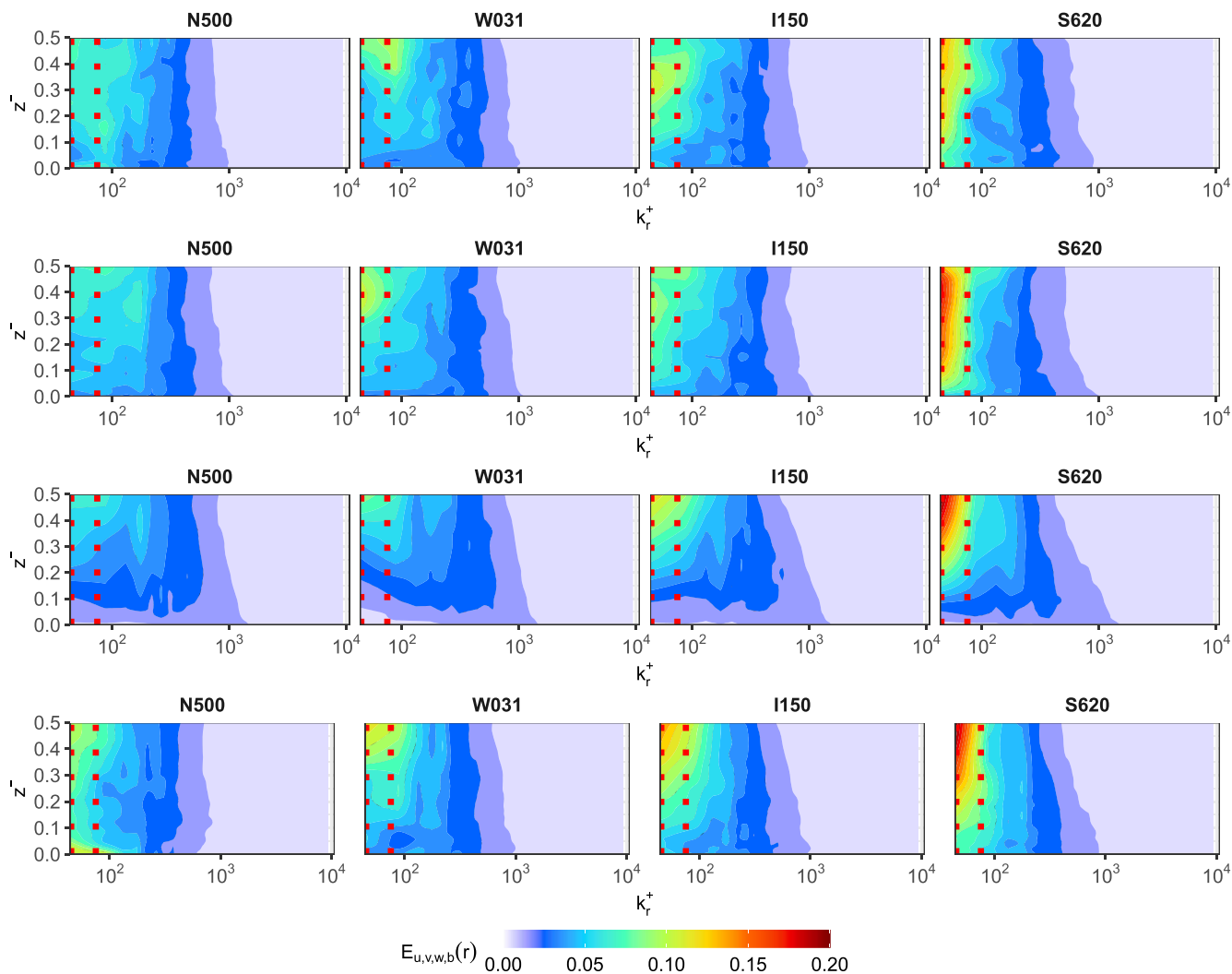
FIGURE 8   Radial spectra for the wind-velocity components u (first line) and v (second line), w (third line), and buoyancy b (fourth line) at $ft \approx 9.5$. Each column indicates different stability intensities; from left to right, these are neutral-N500, weakly stable-W031, intermediate-I150, and strong stable -S620. The vertical red dashed lines represents 2 (right) and 5δ (left) [Colour figure can be viewed at wileyonlinelibrary.com]

from the S620 simulation approach the expression proposed by Mortarini *et al.* (2019) for nonmeandering cases (Figure 6, black dashed line).

5 | FLOW STRUCTURES

In Figures 4b and 5a,b, it was shown that the average profiles show an increasingly pronounced behaviour on moving from the neutral reference state towards stronger stabilities. It is therefore important to address whether the differences are related to the occurrence of meandering in more stable simulations.

Autocorrelation functions and spectra for the wind velocity components are often used to investigate turbulent and nonturbulent properties in the ABL. They play a

central role in determining the temporal and spatial scales of turbulence. In addition, they provide a fundamental tool for identifying oscillatory motions in the velocity and buoyancy fields. For a general stationary process c, the autocorrelation function, $R_c(\xi)$, is defined as

$$R_c(\xi) = \frac{\langle c(x + \xi)c(\xi)\rangle}{\sigma_c^2}, \tag{16}$$

where ξ is the spacial lag and σ_c^2 is the variance. For fully developed turbulence, Taylor's statistical diffusion theory (Taylor, 1921) predicts a simple exponential decay for the velocity autocorrelation functions. However, large low-frequency oscillations of the wind velocity components and buoyancy have often been observed during strongly stratified conditions. Such motions can be
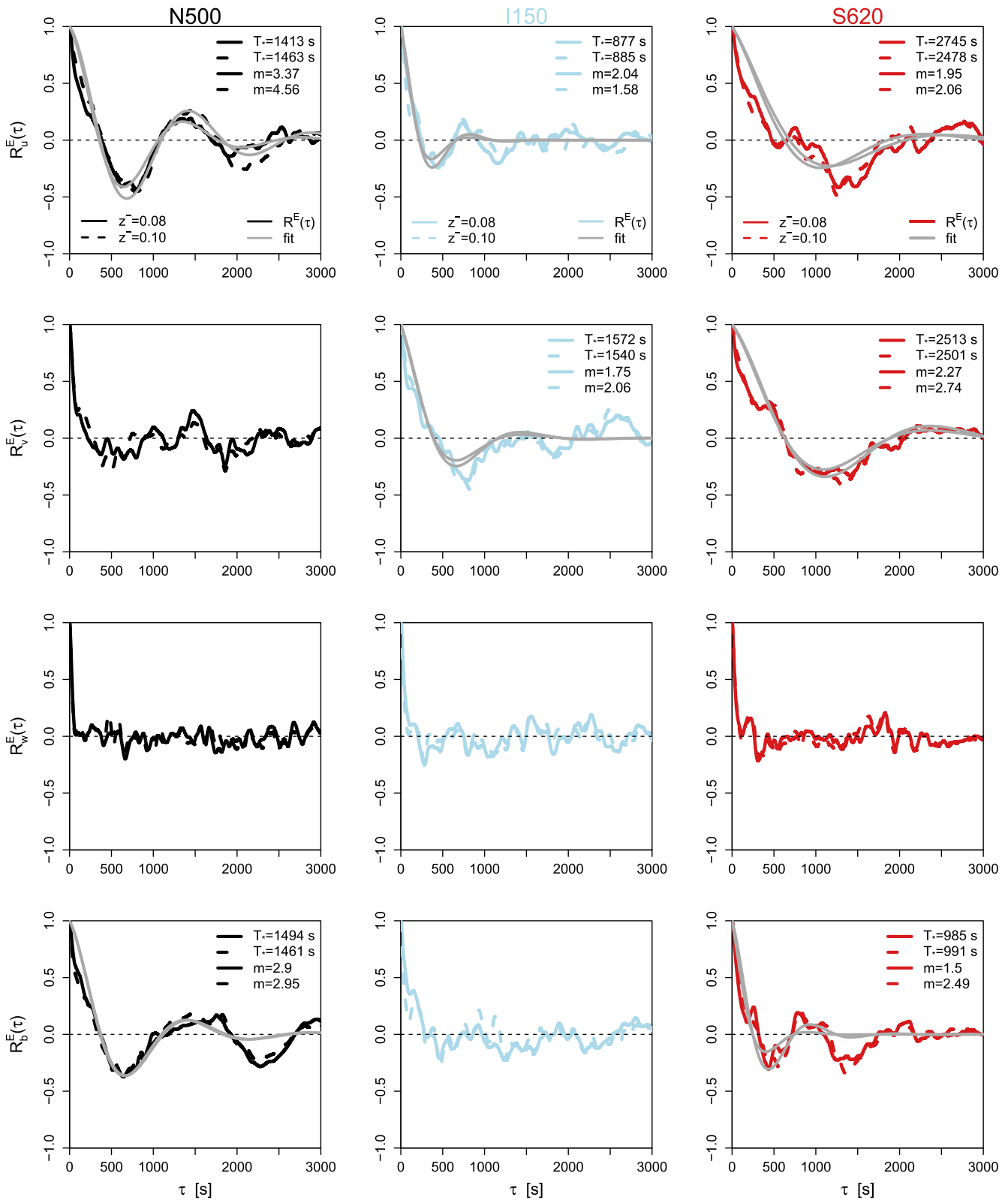
FIGURE 9 Temporal EAFs ($R^E(\tau)$) for the wind-velocity components u (first line) and v (second line), w (third line), and buoyancy b (fourth line) obtained in the centre of horizontal domain in the inner layer at $z^- \approx 0.08$ (continuous lines) and 0.10 (dashed lines) $ft \approx 9.5$. Grey lines represent the theoretical formulation proposed by Anfossi *et al.* (2005) (Equation 17). Each column indicates different stability intensities; from left to right, these are neutral-N500, intermediate-I150, and strong stable-S620 [Colour figure can be viewed at wileyonlinelibrary.com]
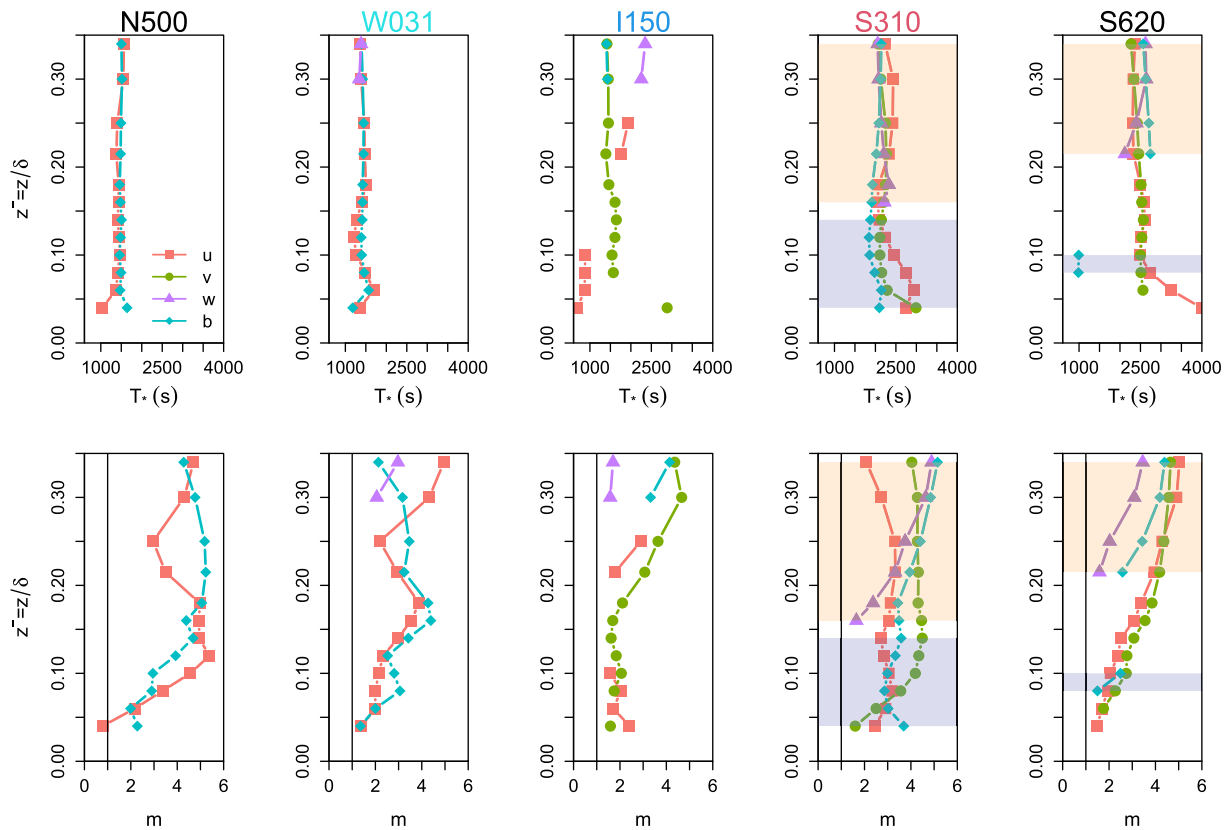
FIGURE 10   Vertical profiles of the meandering time-scale (T_*, top) from Equation (18) and the looping parameter (m, bottom) for the three wind velocity components and buoyancy for the simulated cases at $ft \approx 9.5$ [Colour figure can be viewed at wileyonlinelibrary.com]

recognized by a clear negative lobe (the first negative minimum) in the Eulerian autocorrelation functions (Anfossi *et al.*, 2005; Mortarini *et al.*, 2016b; Mortarini *et al.*, 2019; Urbancic *et al.*, 2021).

Figure 7 shows the Eulerian autocorrelation functions for the wind velocity components and buoyancy at the last simulation time step. Each column represents a different stability intensity, from neutral (N500) to strongly stable (S620) cases. Stability has a large influence on the magnitude and position of the negative lobe. With increasing stability, large oscillatory events characterized by accentuated negative lobes are observed in the wind velocity components and buoyancy. In particular, vertical oscillations occur above the maximum wind speed in the outer layer at $z^- \approx 0.2$ and could be related to gravity-wave activity (Garcia-Villalba and Del Alamo, 2011; Ansorge and Mellado, 2016). On the other hand, the oscillations in the horizontal wind components occur more frequently with strong stabilities in regions close to the wall. The negative lobe is associated with the existence of a peak in the spectrum in the low-frequency region (Figure 8). The peak in the low-frequency region is distinct and more energetic in strong stable cases, which have a length-scale of 2–5δ (red dashed lines in Figure 8), in agreement with Ansorge and Mellado (2016). The spectra also provide

evidence that the energy maximum for the large-scale vertical oscillations at $z^- \approx 0.2$ is damped. As the flow becomes more stable, the spectra for the horizontal components and buoyancy increase the energy peak in low-frequency regions. It seems that the large-scale structures extend downward from the outer layer and penetrate the inner layer as stratification increases. To compare the DNS results with experimental field data, temporal EAFs for the wind velocity components and the buoyancy were evaluated (Figure 9). To describe the oscillatory behaviour in the observed temporal EAFs, the following analytical formulation proposed by Anfossi *et al.* (2005) was considered in the experimental investigations (Cava *et al.*, 2016; Mortarini *et al.*, 2016a; Mortarini *et al.*, 2016b; Cava *et al.*, 2019; Mortarini *et al.*, 2019; Stefanello *et al.*, 2020):

$$R_c(\tau) = e^{-p\tau} \cos(q\tau), \quad (17)$$

where τ is the temporal lag, the parameter p is associated with the turbulence time-scale, and the parameter q is related to the meandering period:

$$T_* = \frac{2\pi}{q}. \quad (18)$$

The ratio between q and p defines the loop parameter $m = q/p$. Low values of this ratio indicate that turbulence

prevails in the oscillatory motions, while large values (>1) indicate that oscillatory motions play an important role in the flow dynamics. A description of the fitting method can be found in Cava *et al.* (2019). Mortarini *et al.* (2016b); Mortarini *et al.* (2016a) used the criterion $m \geq 1$ for the horizontal wind velocity components and temperature (here buoyancy) simultaneously to identify meandering episodes.

Oscillatory behaviour is observed in the temporal EAF under neutral stratification in the *u*-wind velocity component and buoyancy (passive scalar), presenting $T_* \approx 1,400$ s. The presence of such large-scale modes represents a feature of turbulent Ekman flow and is also described in the neutral limit by Ansorge and Mellado (2016). As the stability effect increases, the oscillatory behaviour in the EAFs becomes more evident. For the most stable cases (S310, not shown, and S620), it is possible to observe a clear negative lobe in the EAF and the condition $m_{u,v,b} \geq 1$. The time-scales evaluated using Equation (18) characterize periods of meandering-like structures ranging from 2,454–2,744 s for T_{*u}, 2,109–2,513 s for T_{*v}, and finally 985–1,979 s for T_{*b}. These periods present magnitudes comparable with those obtained employing observational time series during very stable meandering conditions (Anfossi *et al.*, 2005; Moor *et al.*, 2015; Mortarini and Anfossi, 2015; Mortarini *et al.*, 2016a; Mortarini *et al.*, 2016b; Cava *et al.*, 2019; Mortarini *et al.*, 2019; Stefanello *et al.*, 2020; Urbancic *et al.*, 2021). The aforementioned studies found mean values of T_{*u} ranging from 1,322–2,201 s, T_{*v} ranging from 1,044–2,204 s, and T_{*T} ranging from 1,468–1,779 s over the distinct experimental sites. The results are summarized in Figure 10, where T_* and m for all variables in the range $0.04 \leq z^- \leq 0.34$ are shown. The criterion for meandering proposed by Mortarini *et al.* (2016a); Mortarini *et al.* (2016b), $m_{u,v,b} \geq 1$, is met in the simulation S320 in the range $z^- = 0.04$–0.14 and for simulation S620 in the range $z^- = 0.08$–0.1. Nevertheless, meandering-like oscillations occur for specific variables in other cases, being more common in more stable simulations, as shown in Figure 10. Oscillations in the vertical velocity component are observed at levels above the layer where meandering were found, possibly indicating the presence of gravity-wave activity at these higher levels, as previously conjectured by Ansorge and Mellado (2016).

6 | CONCLUSION

In this study, large-scale nonturbulent oscillations in the horizontal wind velocity components and buoyancy were investigated using DNS of an Ekman flow with increasing stable stratification effects. Emphasis is given to characterizing the large scales structures dominant at very stable stability as horizontal meandering modes. For this purpose, vertical profiles of turbulent and mean flow quantities, spatial EAF, and spatial–spectral analysis of the main flow variables have been addressed.

In the case of strong stability, large laminar patches appear in the near-wall region in the vicinity of the turbulent regions, characterized by a low intensity of u_*/G. The simulations have shown that large-scale horizontal wind oscillations can be observed near the wall when the stable stratification is strong enough to suppress vertical turbulent activity. The presence of such horizontal wind oscillations is associated with small values of the ratio between the vertical wind velocity variance and the horizontal wind velocity variances. The TKE has been shown to decrease with stability until it reaches an intermediate stratification intensity, which is due to the reduction of small-scale turbulent activity. However, in the most stable cases, the TKE increases and exceeds the value observed in the neutral case. Such a TKE increase is due mainly to contributions from large-scale oscillations of the horizontal wind components. This is illustrated by low-frequency energetic peaks in the spatial spectra of the horizontal wind components and buoyancy, and by corresponding negative lobes in the spatial and temporal EAFs. Such a finding confirms the main hypothesis of the study, that meandering motion arises naturally as the flow stratification intensifies.

The analysis performed has shown that, when oscillatory modes dominate the dynamics of the SBL, the Rotta constant *c*, which expresses the relationship between dissipation and redistribution terms in the prognostic equations of the velocity deviations, is dependent on stability. Such stability dependence agrees with the experimental observations of Mortarini *et al.* (2019) and could be useful to include in weather prediction models.

The present computational setup used to obtain a turbulent Ekman layer over a smooth flat plate does not include all the elements driving a realistic planetary boundary layer. However, the general evolution expected from the flow and the occurrence of large-scale oscillations when exposed to strong stable stratification are successfully captured and reproduced in the present simulations. In particular, despite the differences in terms of Reynolds number and the lack of surface heterogeneities between the DNS and the field data, the results show that the different dynamics and processes in an SBL are comparable with experimental observations even at a qualitative level. The simulations have given a new insight into the dynamics of the SBL, especially when the stratification is large enough and horizontal wind meandering is a dominant mode near the surface.

AUTHOR CONTRIBUTIONS

ACKNOWLEDGEMENTS

ORCID

Michel Stefanello https://orcid.org/0000-0002-6380-3252

Otávio Acevedo https://orcid.org/0000-0003-2606-4726

REFERENCES

Acevedo, O.C., Mahrt, L., Puhales, F.S., Costa, F.D., Medeiros, L.E. and Degrazia, G.A. (2016) Contrasting structures between the decoupled and coupled states of the stable boundary layer. *Quarterly Journal of the Royal Meteorological Society*, 142(695), 693–702.

Anfossi, D., Alessandrini, S., Trini Castelli, S., Ferrero, E., Oettl, D. and Degrazia, G. (2006) Tracer dispersion simulation in low wind speed conditions with a new 2d langevin equation system. *Atmospheric Environment*, 40(37), 7234–7245.

Anfossi, D., Oettl, D., Degrazia, G. and Goulart, l.A. (2005) An analysis of sonic anemometer observations in low wind speed conditions. *Boundary-Layer Meteorology*, 114(1), 179–203.

Ansorge, C. and Mellado, J.P. (2014) Global intermittency and collapsing turbulence in the stratified planetary boundary layer. *Boundary-Layer Meteorology*, 153(1), 89–116.

Ansorge, C. and Mellado, J.P. (2016) Analyses of external and global intermittency in the logarithmic layer of ekman flow. *Journal of Fluid Mechanics*, 805, 611–635.

Bartholomew, P., Deskos, G., Frantz, R.A.S., Schuch, F.N., Lamballais, E. and Laizet, S. (2020) Xcompact3D: an open-source framework for solving turbulence problems on a cartesian mesh. *SoftwareX*, 12, 100550.

Belušić, D. and Güttler, I. (2010) Can mesoscale models reproduce meandering motions? *Quarterly Journal of the Royal Meteorological Society*, 136(648), 553–565.

Bou-Zeid, E., Gao, X., Ansorge, C. and Katul, G.G. (2018) On the role of return to isotropy in wall-bounded turbulent flows with buoyancy. *Journal of Fluid Mechanics*, 856, 61–78.

Carvalho, J.C., Marco Tullio, M.B. and Vilhena, D. (2005) Pollutant dispersion simulation for low wind speed condition by the ils method. *Atmospheric Environment*, 39(34), 6282–6288.

Cava, D., Mortarini, L., Giostra, U., Richiardone, R. and Anfossi, D. (2016) A wavelet analysis of low wind speed submeso motions in a nocturnal boundary layer. *Quarterly Journal of the Royal Meteorological Society*, 143, 661–669.

Cava, D., Mortarini, L., Anfossi, D. and Giostra, U. (2019) Interaction of submeso motions in the antarctic stable boundary layer. *Boundary-Layer Meteorology*, 171(2), 151–173.

Chorin, A.J. (1968) Numerical solution of the Navier-Stokes equations. *Mathematics of Computation*, 22(104), 745–762.

Coleman, G.N. (1999) Similarity statistics from a direct numerical simulation of the neutrally stratified planetary boundary layer. *Journal of the Atmospheric Sciences*, 56(6), 891–900.

Coleman, G.N., Ferziger, J.H. and Spalart, P.R. (1992) Direct simulation of the stably stratified turbulent ekman layer. *Journal of Fluid Mechanics*, 244, 677–712.

Coleman, G.N., Ferziger, J.H. and Spalart, P.R. (1990) A numerical study of the turbulent ekman layer. *Journal of Fluid Mechanics*, 213, 313–348.

Dairay, T., Fortuné, V., Lamballais, E. and Brizzi, L.E. (2014) Les of a turbulent jet impinging on a heated wall using high-order numerical schemes. *International Journal of Heat and Fluid Flow*, 50, 177–187.

Dairay, T., Lamballais, E., Laizet, S. and Vassilicos, J.C. (2017) Numerical dissipation vs. subgrid-scale modelling for large eddy simulation. *Journal of Computational Physics*, 337, 252–274.

Deskos, G., Laizet, S. and Piggott, M.D. (2019) Turbulence-resolving simulations of wind turbine wakes. *Renewable Energy*, 134, 989–1002.

Deusebio, E., Boffetta, G., Lindborg, E. and Musacchio, S. (2014) Dimensional transition in rotating turbulence. *Physical Review E*, 90(2), 023005.

Flores, O. and Riley, J.J. (2011) Analysis of turbulence collapse in the stably stratified surface layer using direct numerical simulation. *Boundary-Layer Meteorology*, 139(2), 241–259.

Flores, O. and Riley, J.J. (2018) Energy balance in stably-stratified, wall-bounded turbulence. In: Clercx, H. and van Heijst, G. (Eds.) *Mixing and Dispersion in Flows Dominated by Rotation and Buoyancy*. Cham: Springer, pp. 89–99.

Frantz, R.A.S., Deskos, G., Laizet, S. and Silvestrini, J.H. (2021) High-fidelity simulations of gravity currents using a high-order finite-difference spectral vanishing viscosity approach. *Computers & Fluids*, 221, 104902.

Garcia-Villalba, M. and Del Alamo, J.C. (2011) Turbulence modification by stable stratification in channel flow. *Physics of Fluids*, 23(4), 045104.

Garg, R.P., Ferziger, J.H., Monismith, S.G. and Koseff, J.R. (2000) Stably stratified turbulent channel flows. I. Stratification regimes and turbulence suppression mechanism. *Physics of Fluids*, 12(10), 2569–2594.

Goulart, A.G.O., Degrazia, G.A., Acevedo, O.C. and Anfossi, D. (2007) Theoretical considerations of meandering winds in simplified conditions. *Boundary-Layer Meteorology*, 125(2), 279–287.

He, P. and Basu, S. (2015) Direct numerical simulation of intermittent turbulence under stably stratified conditions. *Nonlinear Processes in Geophysics*, 22(4), 447–471.

Iman Gohari, S.M. and Sarkar, S. (2017) Direct numerical simulation of turbulence collapse and rebirth in stably stratified ekman flow. *Boundary-Layer Meteorology*, 162(3), 401–426.

Jiménez, J., Hoyas, S., Simens, M.P. and Mizuno, Y. (2009) Comparison of turbulent boundary layers and channels from direct numerical simulation. In: Sung, H.J. and Choi, H. (Eds.) *Sixth International Symposium on Turbulence and Shear Flow Phenomena*. Danbury, CT: Begell House Inc.

Kravchenko, A.G. and Moin, P. (1997) On the effect of numerical errors in large eddy simulations of turbulent flows. *Journal of Computational Physics*, 131(2), 310–322.

Laizet, S. and Lamballais, E. (2009) High-order compact schemes for incompressible flows: a simple and efficient method with quasi-spectral accuracy. *Journal of Computational Physics*, 228(16), 5989–6015.

Laizet, S. and Li, N. (2011) Incompact3d: a powerful tool to tackle turbulence problems with up to O(10^5) computational cores. *International Journal for Numerical Methods in Fluids*, 67(11), 1735–1757.

Lan, C., Liu, H., Li, D., Katul, G.G. and Finn, D. (2018) Distinct turbulence structures in stably stratified boundary layers with weak and strong surface shear. *Journal of Geophysical Research: Atmospheres*, 123(15), 7839–7854.

Lee, S., Iman Gohari, S.M. and Sarkar, S. (2020) Direct numerical simulation of stratified ekman layers over a periodic rough surface. *Journal of Fluid Mechanics*, 902, A25.

Lele, S.K. (1992) Compact finite difference schemes with spectral-like resolution. *Journal of Computational Physics*, 103(1), 16–42.

Luhar, A.K. (2012) Lagrangian particle modeling of dispersion in light winds. In: Lin, J., Brunner, D., Gerbig, C., Stohl, A., Luhar, A. and Webley, P. (Eds.) *Lagrangian Modeling of the Atmosphere*. New York, NY: Wiley, pp. 37–52.

Luhar, A.K., Hurley, P.J. and Rayner, K.N. (2009) Modelling near-surface low winds over land under stable conditions: sensitivity tests, flux-gradient relationships, and stability parameters. *Boundary-Layer Meteorology*, 130(2), 249–274.

Mahrt, L. (2014) Stably stratified atmospheric boundary layers. *Annual Review of Fluid Mechanics*, 46, 23–45.

Mahrt, L. and Mills, R. (2009) Horizontal diffusion by submeso motions in the stable boundary layer. *Environmental Fluid Mechanics*, 9(4), 443–456.

Mahrt, L. (1999) Stratified atmospheric boundary layers. *Boundary-Layer Meteorology*, 90(3), 375–396.

Mahrt, L. (2009) Characteristics of submeso winds in the stable boundary layer. *Boundary-Layer Meteorology*, 130(1), 1–14.

Mahrt, L. (2011) The near-calm stable boundary layer. *Boundary-Layer Meteorol*, 140, 343–360. 110.1007/s10546-011-9616-2.

Miyashita, K., Iwamoto, K. and Kawamura, H. (2006) Direct numerical simulation of the neutrally stratified turbulent ekman boundary layer. *Journal of the Earth Simulator*, 6, 3–15.

Moor, L.P., Degrazia, G.A., Stefanello, M.B., Mortarini, L., Acevedo, O.C., Maldaner, S., Szinvelski, C.R.P., Roberti, D.R., Buligon, L. and Anfossi, D. (2015) Proposal of a new autocorrelation function in low wind speed conditions. *Physica A: Statistical Mechanics and its Applications*, 438, 286–292.

Mortarini, L. and Anfossi, D. (2015) Proposal of an empirical velocity spectrum formula in low-wind speed conditions. *Quarterly Journal of the Royal Meteorological Society*, 141(686), 85–97.

Mortarini, L., Cava, D., Giostra, U., Acevedo, O., Nogueira Martins, L.G., Soares de Oliveira, P.E. and Anfossi, D. (2018) Observations of submeso motions and intermittent turbulent mixing across a low level jet with a 132-m tower. *Quarterly Journal of the Royal Meteorological Society*, 144(710), 172–183.

Mortarini, L., Cava, D., Giostra, U., Denardin Costa, F., Degrazia, G., Anfossi, D. and Acevedo, O. (2019) Horizontal meandering as a distinctive feature of the stable boundary layer. *Journal of the Atmospheric Sciences*, 76(10), 3029–3046.

Mortarini, L., Maldaner, S., Moor, L.P., Stefanello, M.B., Acevedo, O., Degrazia, G. and Anfossi, D. (2016a) Temperature auto-correlation and spectra functions in low-wind meandering conditions. *Quarterly Journal of the Royal Meteorological Society*, 142, 1881–1889.

Mortarini, L., Stefanello, M., Degrazia, G., Roberti, D., Castelli, S.T. and Anfossi, D. (2016b) Characterization of wind meandering in low-wind-speed conditions. *Boundary-Layer Meteorology*, 161, 1–18.

Nappo, C.J. (2013) *An Introduction to Atmospheric Gravity Waves*. Cambridge, MA: Academic Press.

Nieuwstadt, F.T.M. (2005) Direct numerical simulation of stable channel flow at large stability. *Boundary-Layer Meteorology*, 116(2), 277–299.

Oettl, D., Goulart, A., Degrazia, G. and Anfossi, D. (2005) A new hypothesis on meandering atmospheric flows in low wind speed conditions. *Atmospheric Environment*, 39(9), 1739–1748.

Pope, S.B. (2000) *Turbulent Flows*. Cambridge: Cambridge University Press.

Qian, W. and Venkatram, A. (2011) Performance of steady-state dispersion models under low wind-speed conditions. *Boundary-Layer Meteorology*, 138(3), 475–491.

Rotta, J.C. (1951) Statistische theorie nichthomogener turbulenz. *Zeitschrift für Physik*, 129(6), 547–572.

Shah, S.K. and Bou-Zeid, E. (2014) Direct numerical simulations of turbulent ekman layers with increasing static stability: modifications to the bulk structure and second-order statistics. *Journal of Fluid Mechanics*, 760, 494–539.

Shingai, K. and Kawamura, H. (2004) A study of turbulence structure and large-scale motion in the ekman layer through direct numerical simulations. *Journal of Turbulence*, 5(13), 1–3.

Steeneveld, G.-J. (2014) Current challenges in understanding and forecasting stable boundary layers over land and ice. *Frontiers in Environmental Science*, 2, 41.

Stefanello, M., Cava, D., Giostra, U., Acevedo, O., Degrazia, G., Anfossi, D. and Mortarini, L. (2020) Influence of submeso motions on scalar oscillations and surface energy balance. *Quarterly Journal of the Royal Meteorological Society*, 146(727), 889–903.

Stiperski, I. and Calaf, M. (2018) Dependence of near-surface similarity scaling on the anisotropy of atmospheric turbulence. *Quarterly Journal of the Royal Meteorological Society*, 144(712), 641–657.

Sun, J., Lenschow, D.H., LeMone, M.A. and Mahrt, L. (2016) The role of large-coherent-eddy transport in the atmospheric surface layer based on cases-99 observations. *Boundary-Layer Meteorology*, 160(1), 83–111.

Taylor, G.I. (1921) Diffusion by continuous movements. *Proceedings of the London Mathematical Society*, 20(1), 196–212.

Tennekes, H. (1984) Similarity relations, scaling laws and spectral dynamics. In: Nieuwstadt, F.T.M. and van Dop, H. (Eds.) *Atmospheric Turbulence and Air Pollution Modelling*. Dordrecht: Springer, pp. 37–68.

Urbancic, G.H., Suomi, I. and Vihma, T. (2021) A general theory for the characterization of submeso-scale motions and turbulence in the atmospheric surface layer. *Quarterly Journal of the Royal Meteorological Society*, 147(734), 660–678.

Vercauteren, N., Boyko, V., Faranda, D. and Stiperski, I. (2019) Scale interactions and anisotropy in stable boundary layers. *Quarterly Journal of the Royal Meteorological Society*, 145(722), 1799–1813.

Vickers, D., Mahrt, L. and Belušić, D. (2008) Particle simulations of dispersion using observed meandering and turbulence. *Acta Geophysica*, 56(1), 234–256.